

# On the contribution of coherent vortices to the two-dimensional inverse energy cascade

By ARMANDO BABIANO AND THOMAS DUBOS

Laboratoire de Météorologie Dynamique/IPSL, Paris, France

(Received 15 January 2004 and in revised form 26 October 2004)

We investigate theoretically and numerically the inverse energy cascade in statistically steady two-dimensional turbulence. We perform a numerical testing of the analytical results proposed by Lindborg (*J. Fluid Mech.* vol. 338, 1999, p. 259), and we show that these predictions are quantitatively verified in the inverse energy cascade provided that the quantities involved in the spatial average computation are also averaged over all directions. Then, we define a simple measurable criterion based on the kinetic energy induced by coherent vortices in physical space. Using this criterion, we introduce more selective analyses of the energy cascade that reveal spatial properties of energy transfers which are concealed by global spatial averages. We conclude that there exist convective fluxes in both physical and scale space that feed the energy cascade processes in strongly energetic regions. In two dimensions, these regions are mostly localized around coherent structures. In the turbulent background, this mechanism manifests itself as a deficit of the kinetic energy and weaker inverse energy transfers.

## 1. Introduction

It is well-established in the theory of geophysical fluid dynamics that the solution of the two-dimensional incompressible Navier–Stokes equation is one of the simplest representations where the diversity of geophysical flows can be observed (Leith 1971; Pedlosky 1979). One reason for this is the natural trend of two-dimensional dynamics to generate organized structures, namely coherent shears and vortices, which contain most of the energy and enstrophy of the system. The interest of studying two-dimensional dynamics is increased at high Reynolds numbers when the flow is turbulent and both the direct enstrophy and the inverse energy cascades are present. In both numerical simulations (Boffetta, Celani & Vergassola 2000) and laboratory experiments (Paret & Tabeling 1997) a global statistical description of two-dimensional turbulent cascades can be achieved using the Kolmogorov–Kraichnan theories which rely on the concept of an inertial range characterized by a constant scale-to-scale transfer rate (Kolmogorov 1941; Kraichnan 1967). However, the coherent vortices typically observed in two-dimensional flows play an important role in the understanding of the spatial flow structure (McWilliams 1984; Elhmaili, Provenzale & Babiano 1993). Coherent vortices act as organizing centres of two-dimensional dynamics and they develop basic inhomogeneities and anisotropic non-local processes not explicitly considered in the Kolmogorov–Kraichnan approach. The role of coherent structures in the complex transfer processes which characterize the two cascades in the physical space remains an open issue.

A common strategy for tackling this problem is to introduce suitable diagnostics and indicators to perform more detailed physical-space studies that are eventually

restricted to either one flow region or another. For example, the direct enstrophy cascade (i.e. the creation of small scales in the vorticity field) crucially depends on how the vorticity gradients are aligned with respect to the straining field (Lapeyre, Hua & Klein 2001). The production of the vorticity gradient by stirring depends on the gradient's local orientation with respect to the compressional axis of the strain-rate tensor. Since vorticity gradients tend to align preferentially in one direction, the enstrophy cascade is locally anisotropic (Protas, Babiano & Kevlahan 1999; Dubos & Babiano 2002). At the same time, the cascade depends on the two-dimensional topology described in terms of the competition between vorticity and strain (Hua & Klein 1998), since the cascade is intensified only in well-structured hyperbolic domains (Dubos & Babiano 2003). These strain-dominated domains usually surround coherent vortices where the local kinetic energy is larger than the mean kinetic energy of the flow (Elhmaidi *et al.* 1993). Furthermore, the presence of coherent vortices is probably necessary for the development of the inverse energy cascade to large scales in both decaying and forced two-dimensional turbulence. This property, typically observed in numerical simulations (Maltrud & Vallis 1991), is also confirmed in laboratory experiments (Paret & Tabeling 1998). One of the main conclusions of Paret & Tabeling (1998) is that even if “the role of coherent structures in the inverse energy cascade is an open issue” in forced two-dimensional turbulence, “the cascade is none the less driven by an aggregation process of these structures”. The important point here is to clarify precisely how coherent vortices modify the inverse energy transfers.

The purpose of the present contribution is to address this question on statistically steady turbulence using data obtained from direct numerical simulation of incompressible two-dimensional flow. First, we numerically investigate analytical results proposed in Lindborg (1999) for the two-dimensional inverse energy cascade. These results represent an extension to the two-dimensional case of the standard relations between energy transfer rate and third-order statistics of longitudinal and transverse velocity increments (Landau & Lifshitz 1971). Diagnostics used will be obtained from global spatial averages in the manner of the standard formulation of the theory. We will show that all theoretical predictions are verified provided that quantities involved in the spatial average computation are also averaged over all directions. We then refine this global approach and introduce one-point and two-point energy balance equations that are local in space. These balance equations involve both spatial and scale-to-scale transfers as a function of time and location. On average over the flow domain, the spatial convective transfers do not contribute to the energy balance. However, a conditional average with respect to some topological criterion is not constrained to be zero. These transfers are analysed with conditional averages using a selective criterion based on the distribution of the kinetic energy in physical space. We observe that strongly energetic regions not only bound the area surrounding vortices but also the area surrounding vortex-aggregation patches. Our study produces two main results. First, it appears that convective transfers in physical space are consistently directed inwards in strongly energetic regions and directed outwards in regions with low energy (background turbulent field). Secondly, stronger scale-to-scale energy transfers are found in strongly energetic regions. This locally enhanced inverse energy cascade is fed by spatial energy transfers from weakly energetic regions to strongly energetic regions.

The paper is organized as follows. After a brief review of basic Lindborg's analytical results in §2, we define in §3 one-point and two-point diagnostics for the energy transfers. In §4 we present our two-dimensional numerical simulations and in §5 we comment the results of our analyses. A discussion follows in §6.

## 2. Lindborg's relations in two-dimensional inertial cascades

An important advance in the statistical description of two-dimensional cascades forced at small scales has been made by Lindborg (1999).† He proposes a two-dimensional version of Landau's isotropic relation (Landau & Lifshitz 1971) for the third-order moments of the velocity increments

$$\langle \delta u_{\parallel} \delta u_{\perp} \delta u_{\perp} \rangle = \frac{l}{3} \frac{d}{dl} \langle \delta u_{\parallel} \delta u_{\parallel} \delta u_{\parallel} \rangle, \quad (2.1)$$

where  $l$  is the two-point separation vector,  $u_{\parallel}(\mathbf{x}) = \mathbf{u}(\mathbf{x}) \cdot \mathbf{l}/l$  and  $u_{\perp}(\mathbf{x}) = \mathbf{u}(\mathbf{x}) \times \mathbf{l}/l$  denote velocity components longitudinal and transverse to  $l$  respectively,  $\delta u_{\parallel, \perp}$  refers to the corresponding velocity increment and  $\mathbf{x}$  is the position in space. Here, it is assumed that not only are the scalar quantities isotropic but also the third-order velocity increments tensor (Lindborg 1999). The former assumption is clearly fulfilled when quantities involved in the spatial average computation are averaged over all directions, so that  $\langle \cdot \rangle$  refers to the average at time  $t$  over both the position vectors  $\mathbf{x}$  and directions  $l/l$ . The isotropy of the tensor has been proved in three dimensions to be the consequence of an averaging procedure over all directions (Nie & Tanveer 1999). The numerical results shown in § 5 suggest the same property in two-dimensions.

In terms of two-dimensional turbulent cascades, the two-point diagnostic derived from the two-dimensional Navier–Stokes equation yields for incompressible flow

$$\left\langle \left( \frac{\mathbf{l}}{l} \cdot \delta \mathbf{u} \right) (\delta \mathbf{u} \cdot \delta \mathbf{u}) \right\rangle = \langle \delta u_{\parallel} \delta u_{\parallel} \delta u_{\parallel} \rangle + \langle \delta u_{\parallel} \delta u_{\perp} \delta u_{\perp} \rangle = \frac{1}{4} \varepsilon_Z l^3 \quad (2.2)$$

in the enstrophy cascade and

$$\left\langle \left( \frac{\mathbf{l}}{l} \cdot \delta \mathbf{u} \right) (\delta \mathbf{u} \cdot \delta \mathbf{u}) \right\rangle = \langle \delta u_{\parallel} \delta u_{\parallel} \delta u_{\parallel} \rangle + \langle \delta u_{\parallel} \delta u_{\perp} \delta u_{\perp} \rangle = 2 \varepsilon_E l \quad (2.3)$$

in the inverse energy cascade, where  $\varepsilon_Z$  and  $\varepsilon_E$  denote enstrophy and energy transfer rates respectively. Using (2.1), one finds from (2.2) and (2.3) respectively,

$$\langle \delta u_{\parallel} \delta u_{\parallel} \delta u_{\parallel} \rangle = \langle \delta u_{\parallel} \delta u_{\perp} \delta u_{\perp} \rangle = \frac{1}{8} \varepsilon_Z l^3 \quad (2.4)$$

in the enstrophy cascade and

$$\langle \delta u_{\parallel} \delta u_{\parallel} \delta u_{\parallel} \rangle = \frac{3}{2} \varepsilon_E l \quad (2.5)$$

$$\langle \delta u_{\parallel} \delta u_{\perp} \delta u_{\perp} \rangle = \frac{1}{2} \varepsilon_E l \quad (2.6)$$

in the energy cascade. By analogy with the Kolmogorov–Kraichnan predictions, the criterion used to determine the direction of the energy cascade is based on the sign of the left-hand side of (2.3) (see Lindborg 1999 for a more detailed derivation of all these relations in the two-dimensional approximation).

Relation (2.5) expresses a global statistical link between the third-order longitudinal velocity structure function and the scale-to-scale energy transfer rate  $\varepsilon_E$  in a stationary two-dimensional inverse energy cascade. This classical result has been numerically confirmed by Boffetta *et al.* (2000). A new result obtained from the isotropic relation (2.1) is the diagnostic (2.6) that reveals the relative contribution to the energy cascade of the component of the velocity field transverse to the two-point separation vector  $l$ .

† We do not consider the case also analysed by Lindborg where turbulence is in addition forced at largest scales.

We present in §5 an extensive study of all Lindborg's predictions based on global spatial and azimuthal averages. Before embarking on this study, we define in the next section local one-point and two-point energy balances. These balances will be used as a basis for more selective analyses of the energy distribution in physical space and scale-to-scale transfers, as well as the role played by the transverse structure of the velocity field on the exchange of energy between different flow regions and between different scales.

### 3. One-point and two-point diagnostics for the energy balance

#### 3.1. One-point statistics

The evolution equation for the kinetic energy per unit mass  $\mathbf{u} \cdot \mathbf{u}/2$  is obtained by multiplying the two-dimensional Navier–Stokes equation by the velocity  $\mathbf{u}$ , and taking the average over the flow domain  $\mathcal{D}$  of area  $\Sigma_{\mathcal{D}}$ . We have

$$\partial_t I + \mu - q = -\eta, \quad (3.1)$$

where  $I$ ,  $\mu$  and  $q$  denote respectively the mean values over the flow domain of the kinetic energy, dissipation and forcing, all per unit mass. The quantity  $\eta$  is the mean convective energy transfer rate per unit mass through the boundaries of the flow domain  $\mathcal{D}$ . For situations that have adequate boundary conditions, such as periodicity or vanishing velocity at the boundary, the transfer rate  $\eta$  is equal to zero in the flow domain.

We intend to evaluate more-local quantities in order to relate the balance equation (3.1) to the two-dimensional topology. Thus, let  $\mathcal{D}_l$  be a control surface of area  $\Sigma_l$  and typical scale  $l$  centred on  $\mathbf{x}$  in the flow domain  $\mathcal{D}$  (for examples, circles of diameter  $l$  with  $\Sigma_l \ll \Sigma_{\mathcal{D}}$ ). The elementary balance equation of the kinetic energy in the domain  $\mathcal{D}_l$  is given by

$$\partial_t I_l + \mu_l - q_l = -\eta_l, \quad (3.2)$$

where  $I_l$ ,  $\mu_l$  and  $q_l$  denote respectively the mean values of the kinetic energy, dissipation and forcing (per unit mass) in the control surface  $\mathcal{D}_l$  and

$$\eta_l(\mathbf{x}, t) = \frac{1}{\Sigma_l} \oint_{S_l} \left( \frac{\mathbf{u} \cdot \mathbf{u}}{2} + p \right) (\mathbf{u} \cdot \mathbf{n}) \, ds \quad (3.3)$$

is now the convective energy transfer per unit mass through the contour  $S_l$  containing the control surface  $\mathcal{D}_l$ ,  $\mathbf{n}$  is the unit vector normal to the boundary element  $ds$ , and  $p$  is the pressure (Landau & Lifshitz 1971). This term  $\eta_l$  represents the transport in physical space of the kinetic energy at the local velocity  $\mathbf{u}$  and the work of pressure forces. The left-hand side of (3.2) reflects the net local balance between the variation of the kinetic energy and the local contribution of both the dissipation and forcing in the control surface  $\mathcal{D}_l$ . Thus,  $\eta_l(\mathbf{x}, t)$ , which is a function of time  $t$  and position  $\mathbf{x}$ , can be either positive or negative, respectively corresponding to outward and inward energy flux through the contour  $S_l$ . According to (3.2), negative  $\eta_l$  contributes to the growth of the kinetic energy in the control surface  $\mathcal{D}_l$ . Conversely, positive  $\eta_l$  is consistent with the local diminution of kinetic energy. The average of  $\eta_l$  over the flow domain for adequate boundary conditions yields  $\langle \eta_l \rangle = \eta = 0$ . However, a conditional average of  $\eta_l$  with respect to a topological criterion is not constrained to be zero. The pertinent question is whether there is a correlation between the sign of  $\eta_l$  and the two-dimensional topology.

It will turn out that by using a criterion which classifies the flow topology and restricting the statistical analysis of  $\eta_l$  to conditioned statistics, it is possible to

distinguish in the physical space the regions characterized by persistent inward or outward energy convective fluxes.

### 3.2. Two-point statistics

The statistics of velocity differences are the basic tool used to describe the repartition and exchange of energy between the different scales of the flow. Following the approach adopted in the previous section, the purpose of the present section is to derive an analogue of equation (2.3) that is local in space and time, thus providing greater detail on the energy transfers. We focus on the energy transfers produced by the inertial terms of the Navier–Stokes equation, and thus start from the Euler equation:

$$\frac{\partial}{\partial t} \mathbf{u} + \nabla_x \mathbf{u} \cdot \mathbf{u} + \nabla_x p = 0. \quad (3.4)$$

In addition to  $\mathbf{x}$ , consider a second independent spatial variable  $\mathbf{l}$ , define primed fields at position  $\mathbf{x}' = \mathbf{x} + \mathbf{l}$

$$\mathbf{u}'(\mathbf{x}, \mathbf{l}) = \mathbf{u}(\mathbf{x} + \mathbf{l}), \quad p'(\mathbf{x}, \mathbf{l}) = p(\mathbf{x} + \mathbf{l})$$

and define their increment between  $\mathbf{x}'$  and  $\mathbf{x}$ :

$$\delta \mathbf{u} = \mathbf{u}' - \mathbf{u}, \quad \delta p = p' - p.$$

The four functions  $\mathbf{u}'$ ,  $p'$ ,  $\delta \mathbf{u}$ ,  $\delta p$  are functions of two independent spatial variables  $\mathbf{x}$  and  $\mathbf{l}$  (and time). The variable  $\mathbf{x}$  spans the space of *positions* while the variable  $\mathbf{l}$  spans the space of *separations*. Its norm  $l$  is the scale at which we study the fluctuations  $\delta \mathbf{u}$  of the velocity field. As shown in Appendix, the velocity increment evolves according to

$$\frac{\partial}{\partial t} \delta \mathbf{u} + \nabla_x \delta \mathbf{u} \cdot \mathbf{u} + \nabla_l \delta \mathbf{u} \cdot \delta \mathbf{u} + \nabla_l (\delta p - \mathbf{l} \cdot \nabla_x p) = 0. \quad (3.5)$$

Notice that  $\delta \mathbf{u}$  is solenoidal with respect to both  $\mathbf{x}$  and  $\mathbf{l}$ . Multiplying by  $\delta \mathbf{u}$ , we obtain the balance equation for the energy  $\delta \mathbf{u} \cdot \delta \mathbf{u}/2$ :

$$\frac{\partial}{\partial t} \frac{\delta \mathbf{u} \cdot \delta \mathbf{u}}{2} + \nabla_x \cdot \left( \frac{\delta \mathbf{u} \cdot \delta \mathbf{u}}{2} \mathbf{u} \right) + \nabla_l \cdot \left( \left( \frac{\delta \mathbf{u} \cdot \delta \mathbf{u}}{2} + \delta p - \mathbf{l} \cdot \nabla_x p \right) \delta \mathbf{u} \right) = 0, \quad (3.6)$$

where the symbols  $\nabla_x \cdot$  and  $\nabla_l \cdot$  stand for the divergence operators with respect to  $\mathbf{x}$  and  $\mathbf{l}$  respectively.

Equation (3.6) illustrates that the variations of energy of velocity fluctuations  $\delta \mathbf{u} \cdot \delta \mathbf{u}/2$  over the separation vector  $\mathbf{l}$  arise from two types of transfers. First, the evolution rate

$$\varphi_l(\mathbf{x}, t) = \nabla_x \cdot \left( \frac{\delta \mathbf{u} \cdot \delta \mathbf{u}}{2} \mathbf{u} \right) \quad (3.7)$$

expresses the convective transport in physical space at the local velocity  $\mathbf{u}$ . Here, as well as in the preceding paragraph, negative  $\varphi_l$  contributes to the growth of  $\delta \mathbf{u} \cdot \delta \mathbf{u}/2$  and vice versa. Secondly we have transfers  $(\delta \mathbf{u} \cdot \delta \mathbf{u}/2 + \delta p - \mathbf{l} \cdot \nabla_x p) \delta \mathbf{u}$  in separation space  $\mathbf{l}$ . This flux can be divided into two parts: the transport of  $\delta \mathbf{u} \cdot \delta \mathbf{u}/2$  in separation space at velocity  $\delta \mathbf{u}$  and the pressure contribution  $(\delta p - \mathbf{l} \cdot \nabla_x p) \delta \mathbf{u}$ . This contribution may be written in a different form in the literature because  $\nabla_x \cdot (\delta \mathbf{u} \delta p) = \nabla_l \cdot ((\delta p - \mathbf{l} \cdot \nabla_x p) \delta \mathbf{u})$  (see the Appendix). An important point is that its conditional average is found negligible in §5.3.

Furthermore, the separation-space flux has components transverse and longitudinal to the separation vector  $\mathbf{l}$  that play very different roles. They each describe transfers between separations  $\mathbf{l}$  but with the same norm and different orientations in the

transverse case, or with the same orientation and different norms in the longitudinal case. Consequently, only the longitudinal component is retained in the azimuthal integral of the balance equation (3.6). This azimuthal integral can be obtained by first integrating (3.6) over  $\mathbf{l}$  in the centred disk  $\mathcal{D}_l$  of radius  $l$  bounded by the circle  $S_l$ :

$$\frac{\partial}{\partial t} \iint_{\mathcal{D}_l} \frac{\delta \mathbf{u} \cdot \delta \mathbf{u}}{2} d^2 \mathbf{l} + \nabla_x \cdot \iint_{\mathcal{D}_l} \frac{\delta \mathbf{u} \cdot \delta \mathbf{u}}{2} \mathbf{u} d^2 \mathbf{l} + \frac{\partial}{\partial l} \oint_{S_l} \left( \frac{\delta \mathbf{u} \cdot \delta \mathbf{u}}{2} + \delta p - \mathbf{l} \cdot \nabla_x p \right) \delta u_{\parallel} ds = 0, \quad (3.8)$$

then differentiating with respect to  $l$  and taking into account that  $\partial/\partial l \iint_{\mathcal{D}_l} = \oint_{S_l}$ :

$$\frac{\partial}{\partial t} \oint_{S_l} \frac{\delta \mathbf{u} \cdot \delta \mathbf{u}}{2} ds + \nabla_x \cdot \oint_{S_l} \frac{\delta \mathbf{u} \cdot \delta \mathbf{u}}{2} \mathbf{u} ds + \frac{\partial}{\partial l} \oint_{S_l} \left( \frac{\delta \mathbf{u} \cdot \delta \mathbf{u}}{2} + \delta p - \mathbf{l} \cdot \nabla_x p \right) \delta u_{\parallel} ds = 0. \quad (3.9)$$

Similar integrations have been performed in three dimensions by Hill (2002) and by Nie & Tanveer (1999). Note that this derivation avoids the introduction of the polar coordinates  $(l, \theta)$  for  $\mathbf{l}$  and remains valid and practical in three dimensions.

It is beneficial to stress here that the same procedure has been applied to the more simple problem of passive scalar advection and scale-to-scale transfer of scalar variance (Dubos & Babiano 2002). The variance balance derived in Dubos & Babiano (2002) is the local version of Yaglom's equation (Monin & Yaglom 1971). Furthermore, the scalar variance was found to be transported in physical space at velocity  $\mathbf{u}$  and in separation space at velocity  $\delta \mathbf{u}$ . The new term that appears for energy derives from the pressure contribution. Because this term is equal to the  $\mathbf{x}$ -divergence of  $\delta p \delta \mathbf{u}$ , it has zero spatial average. Thus, the spatial and azimuthal average of equation (3.6) gives exactly the left-hand side of the global balance relation (2.3). The other terms come from forcing and dissipation, which we do not consider here, mainly because small-scale viscous dissipation is irrelevant in the two-dimensional inverse energy cascade. Thus equation (3.6) does indeed give a local view of the energy transfers produced by inertial terms. The scale-to-scale transfer rate is described by the scalar

$$\varepsilon_l(\mathbf{x}, t) = \left( \frac{\delta \mathbf{u} \cdot \delta \mathbf{u}}{2} + \delta p - \mathbf{l} \cdot \nabla_x p \right) \frac{\delta u_{\parallel}}{l}, \quad (3.10)$$

where we have divided by  $l$  so that  $\varepsilon_l$  has the physical dimension of an energy transfer rate, like  $\varepsilon_E$ . An inverse energy cascade is by definition directed toward large separations  $l$  and thus corresponds to a positive  $\varepsilon_l$ . We can now take advantage of this detailed balance involving  $\varphi_l$  and  $\varepsilon_l$  defined by (3.7) and (3.10) to analyse energy transfers both in scales and in space.

## 4. Numerical procedure

### 4.1. Numerical experiments

We simulate the motion of an incompressible fluid in a doubly periodic square domain  $\mathcal{D}$  by solving the evolution equation of the vorticity  $\omega$  using a standard pseudo-spectral approximation. The flow is forced at a wavenumber  $k_i$  corresponding to an injection scale of  $l_i = \pi/k_i$ . We will consider two experiments with different resolutions and configurations:

(i)  $1728 \times 1728$  grid resolution forced at wavenumber  $k_i = 40$ ; this simulation is labelled R1728F40 and presents both direct enstrophy and inverse energy cascades in a statistically steady state over a reasonable range of scales.



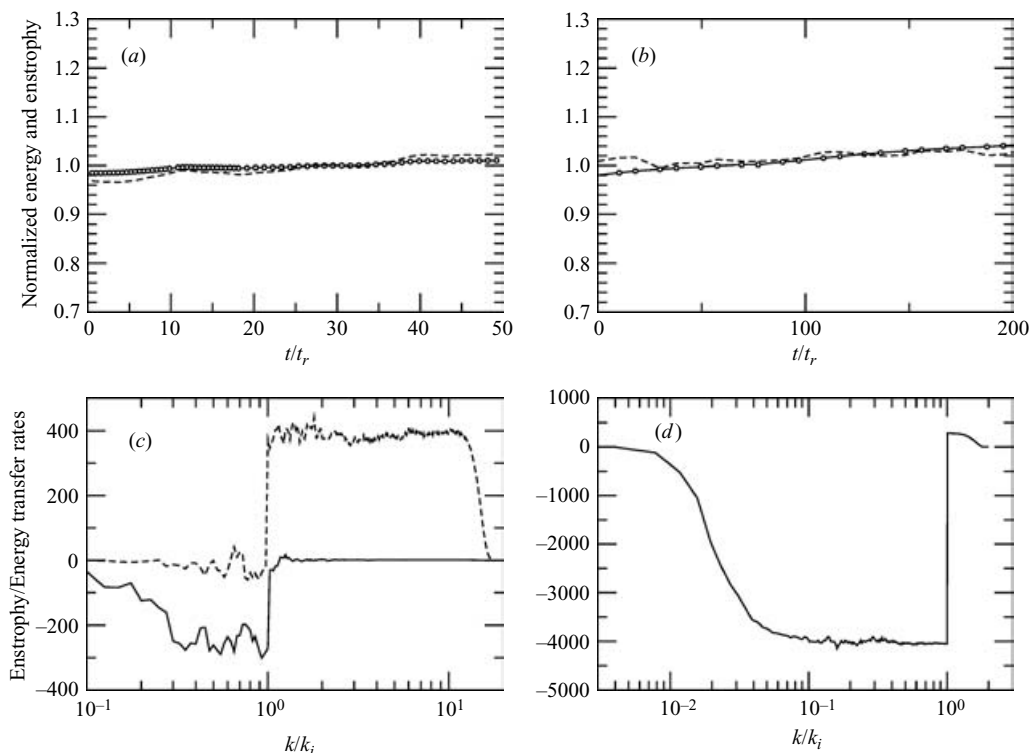


FIGURE 1. Top: normalized kinetic energy (circles) and enstrophy (dashed line) versus time: (a) R1728F40, (b) R1024F256. Bottom: enstrophy (dashed line) and energy (solid line) transfer rates: (c) R1728F40, the enstrophy transfer rate is divided by  $10^3$ , (d) R1024F256.

(ii)  $1024 \times 1024$  grid resolution forced at wavenumber  $k_i = 256$ ; this simulation is labelled R1024F256 and presents a well-developed inverse energy cascade in a statistically steady state.

Forcing is modelled by numerically imposing a constant value on the amplitude of the Fourier mode  $k_i$ . Dissipation includes large-scale linear friction in addition to the iterated Laplacian at small scales:

$$D = -t_c^{-1} (-l_c^2 \nabla^2)^\alpha \omega + t_d^{-1} l_d^{-2} \psi, \quad (4.1)$$

where  $\alpha = 8$ ;  $l_c$  and  $l_d$  are the smallest and the largest resolved scales respectively;  $t_c$  and  $t_d$  are characteristic dissipation times; and  $\psi$  is the stream function. In simulation R1024F256 the iterated Laplacian at small scales is replaced by the strain diffusivity model which conserves energy and has a substantial impact on the energy transfer to large scales, particularly when the enstrophy cascade is almost entirely unresolved and parametrized (Dubos 2001).

Figure 1 shows the behaviour of the most important control characteristics of our numerical simulations. Kinetic energy  $E$  and enstrophy  $Z = \langle \omega^2 \rangle / 2$  are normalized by their corresponding mean values over a time interval of the order of 50 turnover times for R1728F40 and 200 turnover times for R1024F256. The turnover time  $t_r$  is defined by  $t_r = Z^{-1/2}$  ( $Z = 6.5 \times 10^4$ ,  $E = 115$  for R1728F40 and  $Z = 3.4 \times 10^6$ ,  $E = 1700$  for R1024F256). Both simulations are characterized by stationary and scale-independent transfer rates in the inertial ranges. A stationary state is maintained during a time period of  $3 \times 10^4 \Delta t$  with a time step  $\Delta t = 10^{-5}$  for the two simulations.

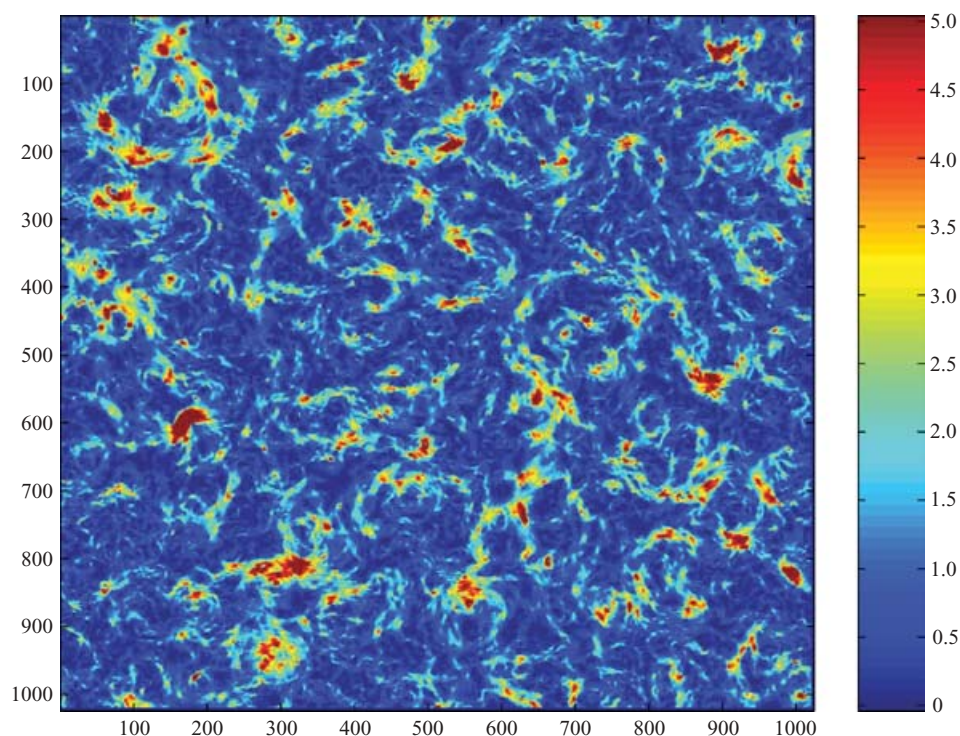


FIGURE 2. Distribution in the physical space of the kinetic energy normalized by the mean kinetic energy of the flow: experiment R1024F256.

#### 4.2. Global and conditional statistics

The erratic character of turbulence makes a statistical treatment of balance equations necessary. A complete (spatial, temporal and azimuthal) averaging procedure leads to Lindborg's Kolmogorov-like relations (2.2)–(2.6). We will show in §5.1 that these relations are well-satisfied even without temporal averaging provided the azimuthal average is performed carefully. The azimuthal average at a given scale  $l$  applied on each position  $\mathbf{x}$  in space includes  $M$  values of the azimuthal angle between 0 and  $2\pi$  on the circle centred at  $\mathbf{x}$ . The interpolation in physical space is performed using a third-order method. A comparison between this procedure and a more precise computation in Fourier space using convolution products shows that statistical convergence is reached for  $M = 14$ .

However, relations (2.2)–(2.6) provide no details on the spatial variability of the cascade process: a less complete spatial averaging procedure will be necessary for this study. Thus, while always performing the azimuthal average, we will also consider conditional averages of the fluxes introduced in the preceding paragraphs, specifically the convective transport rates  $\eta_l$  and  $\varphi_l$  and the scale-to-scale transfer rate  $\varepsilon_l$ . The averages are conditioned on some quantity which is assumed to be representative of the flow topology. Sections 5.2 and 5.3 illustrate that the normalized local kinetic energy  $e(\mathbf{x}) = \mathbf{u} \cdot \mathbf{u} / 2\bar{e}$ , where  $\bar{e}$  refers to the mean kinetic energy of the flow, plays this role rather well: conditional averages with respect to energy depart significantly from the global average and reveal local features of the energy cascade. Figure 2 shows the spatial distribution of the normalized kinetic energy in simulation R1024F256. Energy concentrations correspond to coherent vortices in which the maximum energy



is attained at the injection scale  $l_i = \pi/k_i$  (see Elhmaidi *et al.* 1993 and Paret & Tabeling 1998 for a more detailed discussion). It can also be seen that energy concentrations associated with vortices define large-scale structures of various sizes that are enclosed by energy levels close to two times the mean value  $\bar{e}$  (vortex-aggregation patches).

Let  $\zeta_l$  be the transport rate  $\eta_l$  or  $\varphi_l$  defined by (3.3) and (3.7) respectively. The sign of the total contribution of these transport rates at a given length scale  $l$  and as a function of the kinetic energy is statistically defined by the sign of the conditioned quantity

$$E_\zeta(e) = \sum_{e-\Delta e < e(\mathbf{x}) \leq e+\Delta e} \zeta_l(\mathbf{x}). \quad (4.2)$$

This sum is conditioned on the energy  $e$  so that  $E_\zeta(e)$  reflects the total contribution of all fluxes  $\zeta_l$  observed at given energy level  $e \pm \Delta e$ , where  $\Delta e$  is a constant bin width.

Analogously, we define two partial averages for  $\zeta_l = \eta_l, \varphi_l$  or  $\varepsilon_l$ :

$$\langle \zeta_l \rangle_{e \leq 1} = \frac{1}{N} \sum_{e(\mathbf{x}) \leq 1} \zeta_l(\mathbf{x}), \quad (4.3)$$

$$\langle \zeta_l \rangle_{e > 1} = \frac{1}{N} \sum_{e(\mathbf{x}) > 1} \zeta_l(\mathbf{x}), \quad (4.4)$$

where  $N$  is the total number of points in the simulation box. Strictly speaking, instead of dividing by  $N$ , we should divide  $E_\zeta(e)$  by the number of points for which  $e - \Delta e < e(\mathbf{x}) \leq e + \Delta e$  and also divide  $\langle \zeta_l \rangle_{e \leq 1}$  and  $\langle \zeta_l \rangle_{e > 1}$  by the number of points for which  $e(\mathbf{x}) \leq 1$  and  $e(\mathbf{x}) > 1$  respectively. The convention we have adopted has the advantage of being straightforwardly linked to the global average, so that we have simply  $\langle \zeta_l \rangle = \langle \zeta_l \rangle_{e \leq 1} + \langle \zeta_l \rangle_{e > 1}$  for instance.

## 5. Results

### 5.1. Lindborg's relations: global averages

We focus here on the numerical verification of the isotropic relation (2.1) for the third-order velocity structure functions in both the inverse energy cascade (simulation R1024F256) and the direct enstrophy cascade (simulation R1728F40). Isotropic relation (2.1) is analysed in the form

$$\frac{\langle \delta u_{\parallel} \delta u_{\perp} \delta u_{\perp} \rangle}{\langle \delta u_{\parallel} \delta u_{\parallel} \delta u_{\parallel} \rangle} = \frac{1}{3} \frac{\mathrm{d} \log \langle \delta u_{\parallel} \delta u_{\parallel} \delta u_{\parallel} \rangle}{\mathrm{d} \log l}, \quad (5.1)$$

where as pointed out above  $\langle . \rangle$  refers to the average at time  $t$  over both the position vectors  $\mathbf{x}$  and azimuthal directions  $l/l$ .

In figure 3 we compare the two sides of relation (5.1) by plotting as a function of the normalized length scale  $l/l_i$  the ratio  $\langle \delta u_{\parallel} \delta u_{\perp} \delta u_{\perp} \rangle / \langle \delta u_{\parallel} \delta u_{\parallel} \delta u_{\parallel} \rangle$  (circles) and the logarithmic derivative  $\frac{1}{3} \mathrm{d} \log \langle \delta u_{\parallel} \delta u_{\parallel} \delta u_{\parallel} \rangle / \mathrm{d} \log l$  (dashed line). The relation (5.1) appears to be well-satisfied at all scales. As recognized in Babiano, Basdevant & Sadourny (1985) the scalar relation between longitudinal and transverse velocity increments does not characterize isotropy but is only a consequence of it. The results shown in figure 3 only confirm the previous statement and show that the azimuthal average used in our computation including 14 azimuthal directions  $l/l$  ensures a good statistical 'isotropization'.

Figure 4 represents the corresponding  $\langle \delta u_{\parallel} \delta u_{\parallel} \delta u_{\parallel} \rangle$  and  $\langle \delta u_{\parallel} \delta u_{\perp} \delta u_{\perp} \rangle$  behaviours. At viscous scales, a kinematic scaling with  $l^5$  is expected (Lindborg 1999). Thus, in the

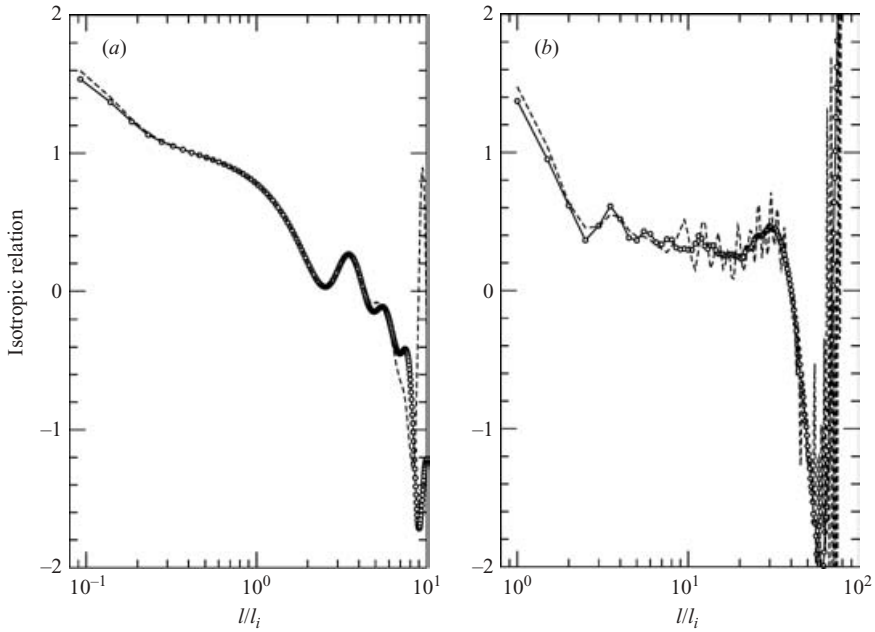


FIGURE 3. Isotropic relation (5.1) as a function of the normalized length scale. (a) Experiment R1728F40; (b) R1024F256. Values of the ratio  $\langle \delta u_{\parallel} \delta u_{\perp} \delta u_{\perp} \rangle / \langle \delta u_{\parallel} \delta u_{\parallel} \delta u_{\parallel} \rangle$  (circles) and of the logarithmic derivative  $\frac{1}{3} d \log \langle \delta u_{\parallel} \delta u_{\parallel} \delta u_{\parallel} \rangle / d \log l$  (dashed line).

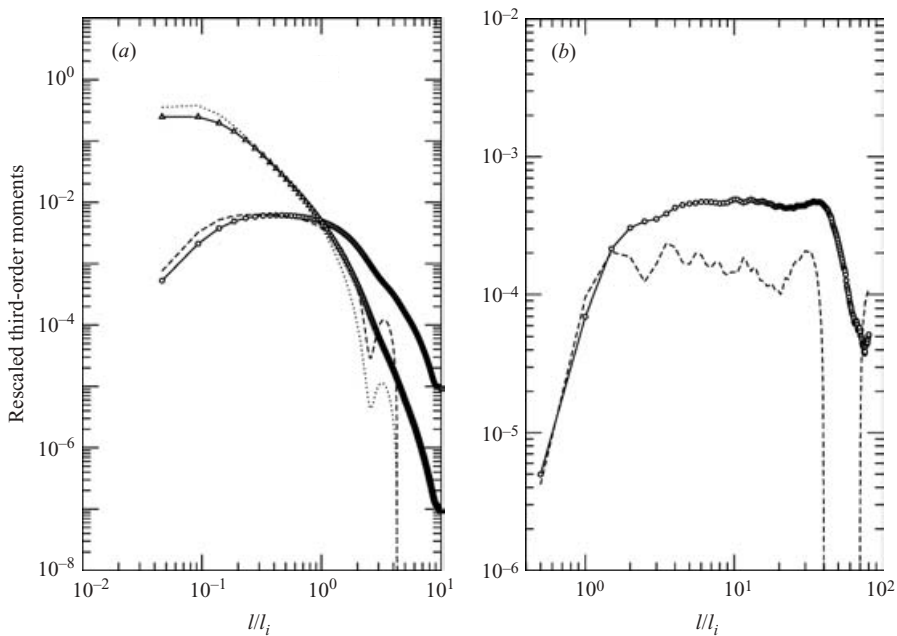


FIGURE 4. Rescaled longitudinal (circles and triangles) and transverse (dashed and dotted lines) third-order structure functions as a function of the normalized length scale. (a) Enstrophy cascade, experiment R1728F40, rescaled by  $l^3$  and  $l^5$ ; (b) energy cascade, experiment R1024F256, rescaled by  $l$ .

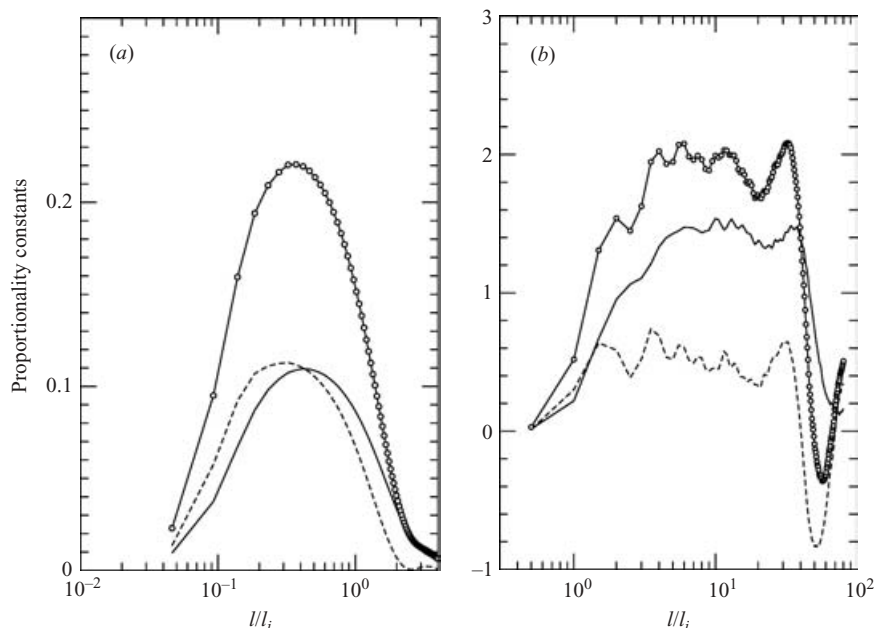


FIGURE 5. Study of the proportionality constants involved in relations (2.2)–(2.6) as a function of the normalized length scale. (a) Experiment R1728F40: relations (2.2) (circles) and (2.4) (solid line, longitudinal; dashed line, transverse); (b) experiment R1024F256: relations (2.3) (circles), (2.5) (solid line) and (2.6) (dashed line).

enstrophy cascade results are rescaled by  $l^3$  (figure 4a, simulation R1728F40; circles and dashed line for  $\langle \delta u_{\parallel} \delta u_{\parallel} \delta u_{\parallel} \rangle$  and  $\langle \delta u_{\parallel} \delta u_{\perp} \delta u_{\perp} \rangle$  respectively) and by  $l^5$  (triangles and dotted line). In the inverse energy cascade results are rescaled by  $l$  (figure 4b, simulation R1024F256). Cubic and linear dependences in the enstrophy and energy cascade ranges as predicted by the theory, as well as the kinematic scaling with  $l^5$  at smallest scales, are well-satisfied. This last result once again gives support to the validity of the computation. A large plateau which follows the linear scaling (2.5) and (2.6) in the inverse energy cascade is observed in figure 4(b). This plateau is consistent with the behaviour of the left-hand side of (5.1) displayed in figure 3(b), which is constant at a value close to  $1/3$ . However, prediction (2.4) in the enstrophy cascade range correlates more weakly with the simulation R1728F40: figure 3(a) displays an approximate plateau around 1, corresponding in figure 4(a) to a short transition through a  $l^3$  scaling. Relation (2.4) in the direct enstrophy cascade has been verified with great precision in a higher-resolution simulation ( $4096 \times 4096$ ) forced at a low wavenumber  $k_i = 4$  (Lindborg & Alvelius 2000). In that setup only the direct enstrophy cascade was simulated. The weak support for equation (2.4) in our case may be attributed to the shorter range of scales over which the enstrophy cascade develops. Our choice of a larger wavenumber  $k_i = 40$  in the R1728F40 experiment is made to simulate both enstrophy and energy cascades over a reasonable range of scales, which should highlight that our observations of the convective and scale-to-scale energy transfer rates are specific to the inverse energy cascade.

In order to study not only scaling exponents but also proportionality constants we computed spectral enstrophy and energy transfer rates  $\varepsilon_Z$  and  $\varepsilon_E$ . We were then able to obtain all constants involved in relations (2.2)–(2.6). The results are displayed in figure 5. All three constants in the energy cascade range are in remarkable agreement

with the values predicted in Lindborg (1999) (figure 5b). However, the results in the enstrophy cascade range (figure 5a) are slightly lower than that expected. All the above results show that what we have observed in our numerical simulations using a global average procedure is indeed a two-dimensional inverse energy cascade as described in §2.

For completeness, let us mention that the same study performed without azimuthal averaging produces an inextricable set of results. In our numerical data, both the sign and the sign change of the non-‘isotropized’ mean third-order moments display an obvious dependence on the direction  $l/l_i$ . This problem is more acute than in three-dimensional turbulence because of the small skewness of two-dimensional velocity increments in inertial ranges (Paret & Tabeling 1998). In Paret & Tabeling (1998), the isotropy of the two-dimensional flow was analysed in terms of the two-dimensional energy spectrum, which is a second-order moment. The authors conclude that the cascade mechanism involves an efficient isotropization of the flow. We find that in the case of third-order moments the situation is less clear. In accordance with these results we will base our further analysis on azimuthal averages.

### 5.2. Conditional one-point statistics

We first present a study of relation (3.2) conditioned by the normalized kinetic energy  $e(\mathbf{x}) = \tilde{u}^2/2\bar{e}$ , where  $\bar{e}$  refers to the mean kinetic energy and  $\tilde{u}^2/2$  is its local mean value over each contour  $S_l$  centred on  $\mathbf{x}$ . According to the elementary balance (3.2), energy fluxes through the boundary of the control surface  $\mathcal{D}_l$  are statistically inward or outward depending on the sign of the conditioned quantity  $E_\eta$  defined by (4.2) (with  $\zeta_l = \eta_l$  defined by (3.3)). Negative  $E_\eta$  correspond to inward energy fluxes and vice versa.

The behaviour of  $E_\eta$  as a function of the normalized kinetic energy  $e$  for normalized scales  $l/l_i = 3, 5$  is presented in figure 6(a) (simulation R1024F256). We observe a positive lobe in the domain  $e < 1$  and a negative lobe in the domain  $e > 1$ . By definition, the average value of  $E_\eta$  is zero, which results in an overall cancellation of these two lobes. It is most important to note that positive and negative values for  $E_\eta$  occur for  $e < 1$  and  $e > 1$  respectively. Hereafter, we will base our conditional analyses on this property.

We now turn to the length-scale dependence of conditional inward and outward convective transport rates  $\eta_l$  defined by (3.3). Figure 6(b) shows the non-conditional  $\langle \eta_l \rangle$  and the conditional  $\langle \eta_l \rangle_e$ , defined as (4.3)–(4.4), as a function of the length scale. The conditional averaging is performed with respect to  $e \leq 1$  (bold dashed lines) or  $e > 1$  (bold solid lines) as is suggested by the shape of  $E_\eta$ . All quantities have been normalized by the global scale-to-scale energy transfer rate  $\varepsilon_E$ . The non-conditional  $\langle \eta_l \rangle$  confirms at all scales the expected zero mean value (dotted line). As a result, values for the conditional  $\langle \eta_l \rangle_e$  are naturally symmetric with respect to the  $\langle \eta_l \rangle = 0$  axis. By definition, the local departure from the equilibrium among energy dissipation, forcing, and time variation terms (left-hand side of (3.2)) is expressed by  $\eta_l$ . The latter is obtained from (3.3) by adding the contributions from the kinetic energy transport (circles) and the work of pressure forces (triangles).

For comparison, figure 6(b) also displays the conditional  $\langle \eta_l \rangle$  for the corresponding random field where all structures have been destroyed by randomizing the phase of Fourier coefficients (thin solid and dashed lines). This last result confirms the role of the two-dimensional spatial structure in the convective energy transfers in the physical space.

We draw two main conclusions from these numerical results. First, it seems that the mean kinetic energy is a criterion to discriminate between positive and negative

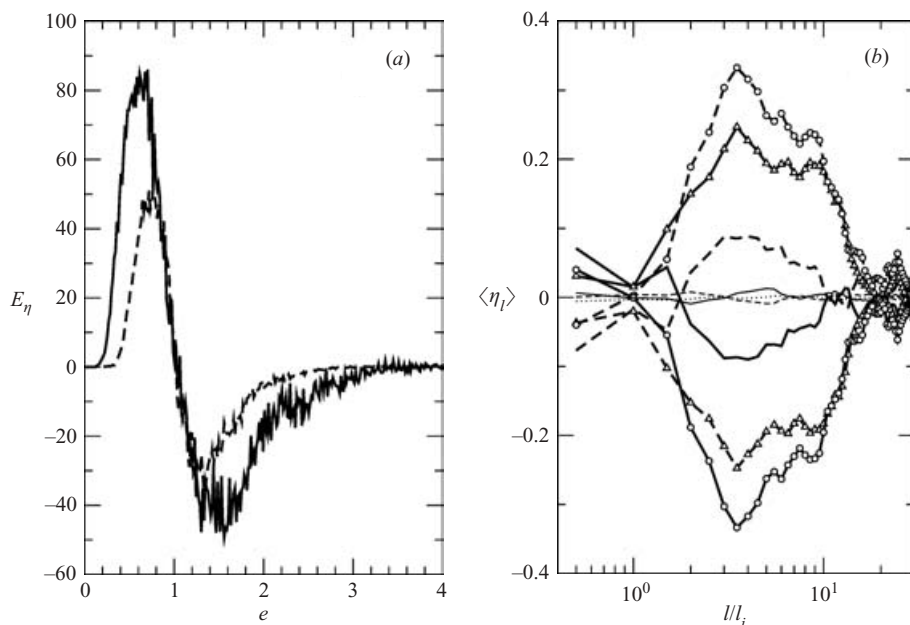


FIGURE 6. Conditional one-point statistics for experiment R1024F256. (a) Behaviour of  $E_\eta$  as a function of the normalized kinetic energy for two separations  $l/l_i = 3$  (solid line), 5 (dashed line); (b) behaviours of  $\langle \eta_l \rangle$  (dotted line) and  $\langle \eta_l \rangle_e$  (bold lines) normalized by  $\varepsilon_E$  as a function of the normalized length scale; kinetic energy (circles) and pressure (triangles) contributions. See text for complete description of line styles.

balance in the relation (3.2). Secondly, persistent inward energy fluxes ( $E_\eta < 0$ ) occur in strongly energetic regions, whereas outward fluxes ( $E_\eta > 0$ ) characterize the low energetic turbulent background. Thus, the competition between energy concentration and dissipation predominantly occurs in the strongly energetic regions. These regions correspond to the hyperbolic (strain-dominated) domains at the periphery of coherent structures as well as the moderately elliptic (vorticity-dominated) domains which surround vortex cores (Elhmaidi *et al.* 1993). Since energy dissipation processes are particularly dominant at large scales in two-dimensional flows one may conclude that the main effect of inward fluxes is to maintain and reinforce high energy levels at the expense of the turbulent background. This picture is consistent with the trend towards the concentration of energy observed in two-dimensional turbulent flows. In our numerical experiment,  $\langle \eta_l \rangle_e$  appears as a non-negligible fraction of  $\varepsilon_E$ :  $\langle \eta_l \rangle \simeq \pm 0.1 \varepsilon_E$  (see figure 6b).

### 5.3. Conditional two-point statistics

Figure 7 displays  $E_\varphi(e)$  for the transport rate  $\varphi_l$  which is defined by (3.7), for two separations  $l/l_i = 3, 5$  lying in the energy cascade range. The quantity  $E_\varphi$  is analogous to the total flux  $E_\eta$  studied in § 5.2. Just as before, although less clearly,  $E_\varphi$  tends to be positive (outward fluxes) for small kinetic energies  $e$  and negative (inward fluxes) for larger kinetic energies, with the sign change occurring around the average kinetic energy. According to the balance equation (3.6), this again implies that the convective transport in physical space tends to drag the energy  $\delta \mathbf{u} \cdot \delta \mathbf{u} / 2$  away from low-energy regions (turbulent background) and toward high-energy regions (surrounding vortices and vortex-aggregation patches).



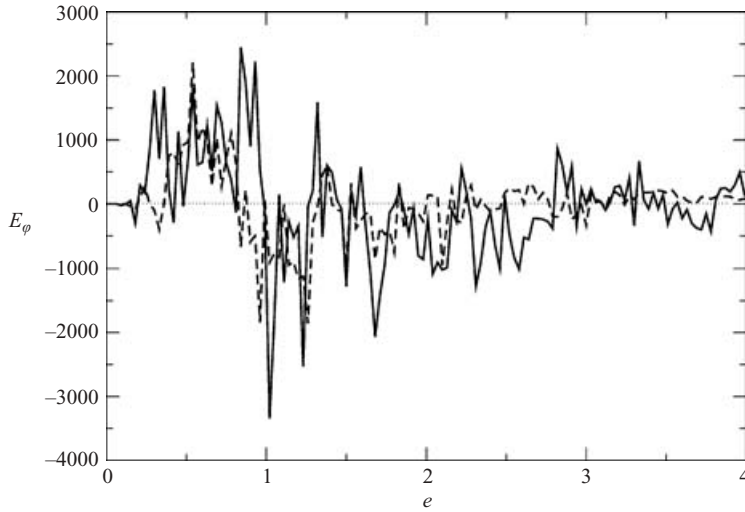


FIGURE 7. Conditional two-point statistics. Behaviour of  $E_\varphi$  as a function of the normalized kinetic energy for two separations  $l/l_i = 3$  (solid line), 5 (dashed line). Experiment R1024F256.

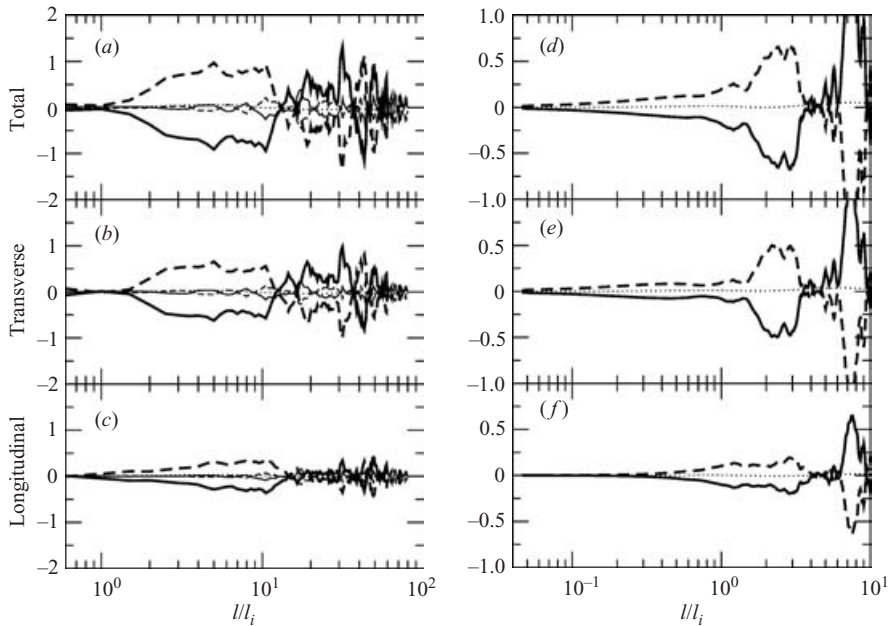


FIGURE 8. Conditional two-point statistics. Behaviour of  $\langle \varphi_l \rangle$  (dotted line),  $\langle \varphi_l \rangle_e$  (bold dashed line:  $e \leq 1$ ; bold solid line:  $e > 1$ ) and corresponding longitudinal and transverse contributions. (a, b, c) Experiment R1024F256; (d, e, f) experiment R1728F40.

As in § 5.2, we now analyse partial averages (4.3)–(4.4) for the transport rate  $\varphi_l$  defined by (3.7) as a function of the length scale, as shown in figure 8. Thus, the conditional averaging is now simply taken with respect to the conditions  $e \leq 1$  (bold dashed line) and  $e > 1$  (bold solid line). We also verified that the spatial average of  $\langle \varphi_l \rangle$  is zero (dotted curve). As a result, the curves corresponding to partial averages

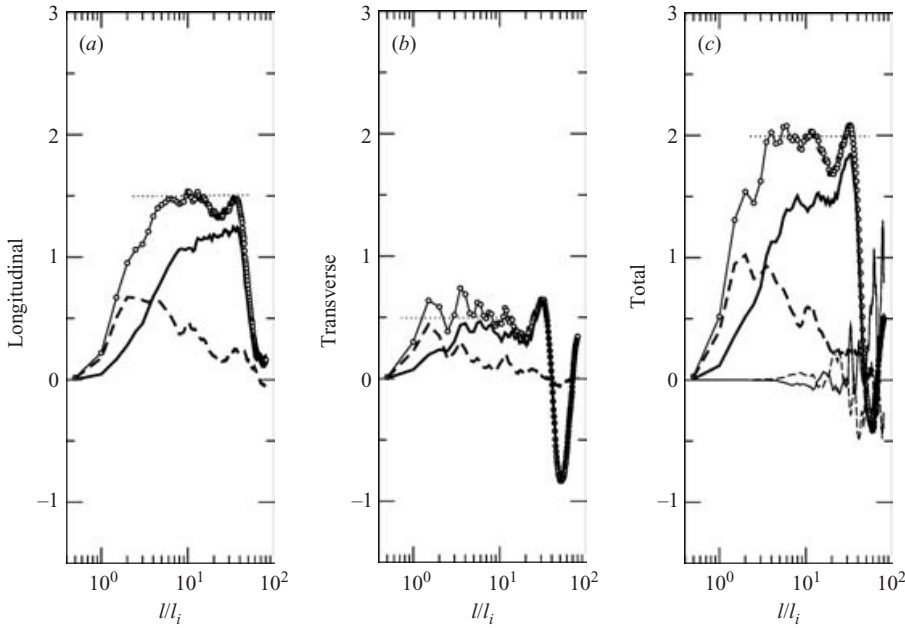


FIGURE 9. Conditional two-point statistics for experiment R1024F256. Behaviour of  $\langle \varepsilon_l \rangle$  (circles) and  $\langle \varepsilon_l \rangle_e$  (bold dashed line:  $e \leq 1$ ; bold solid line:  $e > 1$ ) and corresponding longitudinal and transverse contributions reduced by  $\varepsilon_E/2$ . Universal plateaux discussed in § 5.1 are indicated (dotted line). See text for further details.

are symmetric with respect to the  $\langle \varphi_l \rangle = 0$  axis. The average transport rates are computed in the experiments R1024F256 (left, panels *a*–*c*) and R1728F40 (right, panels *d*–*f*), and are normalized by the corresponding energy transfer rate  $\varepsilon_E$  and plotted as a function of the normalized scale  $l/l_i$ . Furthermore, they are split into the longitudinal contribution  $\varphi_l^\parallel = \nabla_x \cdot (\mathbf{u} \delta u_\parallel^2/2)$  (panels *c*, *f*) and the transverse contribution  $\varphi_l^\perp = \nabla_x \cdot (\mathbf{u} \delta u_\perp^2/2)$  (panels *b*, *e*) which sum to  $\varphi_l = \varphi_l^\perp + \varphi_l^\parallel$  (panels *a*, *d*).

Again, in order to make sure that any observed property is not merely the footprint of the energy spectrum and does result from phase correlations due to spatially coherent structures, we also performed the same computations on a randomized field. The resulting curves (thin solid and dashed lines) fall close to the  $\langle \varphi_l \rangle = 0$  axis, implying that phase correlations are indeed needed for  $\langle \varphi_l \rangle_e$  to maintain a well-defined sign. It can be observed that the conditionally averaged  $\langle \varphi_l \rangle$  takes values with orders of magnitude comparable to  $\varepsilon_E$  inside the inverse cascade range  $1 \leq l/l_i \leq 10$ , while it rapidly decreases to values much smaller than  $\varepsilon_E$  outside this range. This is particularly true in the enstrophy cascade, almost non-existent in the experiment R1024F256 but well-developed in the experiment R1728F40 (panels *d*–*f*). This means that the inverse energy cascade causes an efficient development of the convective transfer rate  $\varphi_l$ . In both experiments, the total  $\langle \varphi_l \rangle_e$  results mainly from the transverse contribution (panels *b* and *e*) while the longitudinal contribution is smaller (panels *c* and *f*). Note that the previously observed sign trend holds consistently throughout the energy cascade range for the three transport rates  $\varphi_l$ ,  $\varphi_l^\parallel$ ,  $\varphi_l^\perp$ .

We complete this analysis of spatial transfer of velocity fluctuations by analysing the corresponding scale-to-scale transfer rate  $\varepsilon_l$  defined by (3.10). We plot in figure 9 the scale-to-scale transfer rate  $\varepsilon_l$  (panel *c*) split into longitudinal contribution  $(\delta u_\parallel)^3/2$

(panel *a*) and transverse contribution  $(\delta u_{\perp})^2 \delta u_{\parallel} / 2$  (panel *b*). Each contribution is summed either over the whole box (circles) or over regions where  $e < 1$  (bold dashed line) or  $e > 1$  (bold solid line). Global averages (circles) have already been displayed in figure 5(*b*). Transfer rates are normalized by  $\varepsilon_E / 2$  and plotted as a function of the normalized scale  $l / l_i$ . We checked that the contribution of the pressure term  $(\delta p - \mathbf{l} \cdot \nabla_x p) \delta u_{\parallel} / l$  is less than 2% of the energy transfer rate  $\varepsilon$  and therefore negligible at all scales in the energy cascade range (figure 9*c*, thin solid and dashed lines). For scales slightly larger than the injection scale, low-energy regions contribute more than high-energy regions to the scale-to-scale transfer (both contributing positively). This implies that the cascade takes place predominantly in low-energy regions at the smallest scales of the energy cascade range. However, efficient scale-to-scale transfers in the turbulent background collapse at larger scales, which is consistent with the development of convective fluxes from the weakly energetic regions to the strongly energetic regions observed in figure 8. As a result, for all scales where Lindborg's relations (2.3), (2.5) and (2.6) are well-verified and indicate a fully developed cascade, the converse is true: high-energy regions contribute significantly more to the inverse energy cascade than low-energy regions. The low-energy contribution even drops to zero before the end of the inertial range.

From these observations it is possible to draw two important conclusions. First, the fully developed inverse energy cascade takes place mainly in highly energetic regions. Secondly, the turbulent background, often considered a passive turbulent medium, in fact plays the role of an energy reservoir for such an inverse cascade process.

## 6. Discussion

We checked numerically the isotropic relation (2.1) and the Kolmogorov-like relations (2.3)–(2.6). Relation (2.1) being very well-verified, we can be confident that our averaging procedure is sufficiently isotropic. This being achieved, the dynamical relations (2.3)–(2.6) and universality of corresponding proportionality constants were found to hold even instantaneously. Nevertheless, there is no reason why the cascade should locally obey these global properties. We thus refined the global statistical analysis in order to take into account the spatial variability of both the energy distribution and the cascade processes. One-point diagnostics for the energy balance consistently confirm the trend towards energy concentration in two-dimensional turbulent flows. In addition, it seems that the mean kinetic energy is a sufficient discriminant to reveal consistent trends in the energy balances that significantly depart from the globally averaged tendency. This is important because energy is a measurable quantity. Our results show that the convective energy flux  $\langle \eta_l \rangle_e$  in the physical space toward high-energy regions has a magnitude of about  $0.1 \varepsilon_E$ . This value may depend on the details of the setup.

Furthermore, using energy as a discriminant we can analyse scale-to-scale transfers involved in the inverse cascade. The balance equation (3.6) provides a local generalization of the statistical relation (2.3). In the resulting picture of the cascade, scale-to-scale transfers (3.10) are supplemented by convective fluxes in physical space (3.7) which complete the local energy balance. Analysing their behaviour as a function of scale and of the local kinetic energy, we derive the following conclusions:

(i) The observed trends reveal the existence of a feeding mechanism of strongly energetic regions surrounding coherent structures compensated by a corresponding deficit of energy  $\delta \mathbf{u} \cdot \delta \mathbf{u} / 2$  in the turbulent background. Our numerical investigations show that the transverse contribution to the convective transfers is consistently

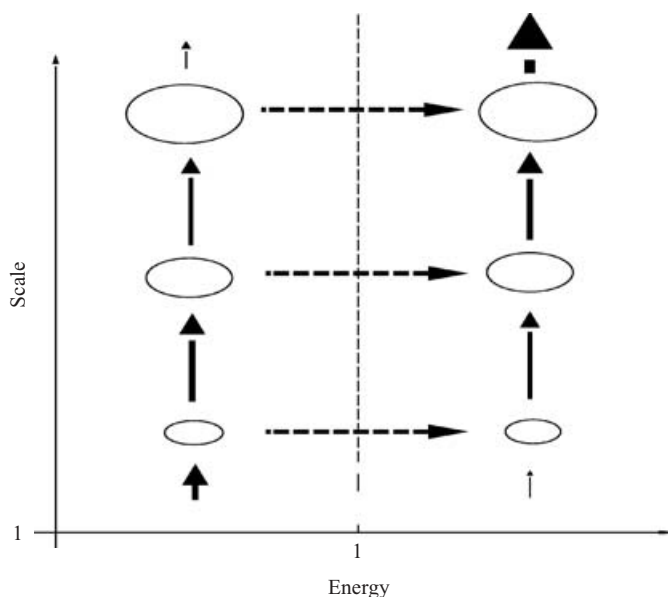


FIGURE 10. Local scenario of two-dimensional inverse energy cascade.

stronger than the longitudinal contribution. This is in contrast to the scale-to-scale transfers, to which the longitudinal structure function predominantly contributes.

(ii) Energy transfer towards large scales in a developed inverse energy cascade predominantly take place in highly energetic regions. This mechanism is however reversed at scales moderately larger than the injection scale, where the inverse energy cascade is principally supported by the turbulent background. In this sense, the turbulent background should be considered to be an active turbulent medium.

These trends are sketched in figure 10. The overall trend of energy transfer toward large scales is refined by spatially distinguishing low-energy regions (left) from high-energy regions (right). These two regions exchange energy to the average benefit of high-energy regions, especially at inertial scales where the energy flux  $\langle \varphi_l \rangle_e$  has a magnitude of about  $\varepsilon_E$  (horizontal arrows). For instance, the energy given by low-energy regions feeds the inverse cascade in high-energy regions. Simultaneously, energy is exchanged at the rate  $\langle \varepsilon_l \rangle_e$  between scales to the average benefit of larger scales (bold vertical arrows). These two trends are connected to each other if we assume statistical steadiness and neglect the contributions of forcing and dissipation to the energy balance. Consequently, the inverse energy cascade in the background, which is rather strong at scales just above the injection scale, collapses at larger scales. Conversely, the observed inter-scale energy flux is stronger in high-energy regions, especially at scales where the cascade is fully developed.

This local scenario, based on our numerical analysis, emphasizes that it would be erroneous to consider that the forced inverse energy cascade in two-dimensional turbulence locally obeys the statistical balance predicted by global statistical theories. Our selective analysis reveals several local-in-space features. This point becomes particularly important when one focuses on a limited region of the flow, as is usually the case in most situations of practical interest. Another question worth exploring is the investigation of the analogous scenario in the framework of decaying two-dimensional turbulence. Finally, an important issue to explore is how much the

two-dimensional local features analysed in the present work are shared by the three-dimensional direct energy cascade.

We are deeply indebted to Suelin Chen who has carefully proofread and corrected this paper. We gratefully acknowledge Patrick Tabeling for useful discussions of these topics. We also wish to thank anonymous referees for helping us improving the clarity and completeness of the paper by their comments and suggestions.

### Appendix. Balance equation for the velocity increments

Writing the Euler equation (3.4) at point  $\mathbf{x} + \mathbf{l}$ , one obtains

$$\frac{\partial}{\partial t} \mathbf{u}' + \nabla_{\mathbf{x}} \mathbf{u}' \cdot \mathbf{u}' + \nabla_{\mathbf{x}} p' = 0. \quad (\text{A } 1)$$

Furthermore, because  $\mathbf{u}$  and  $p$  do not depend on  $\mathbf{l}$  we have

$$\nabla_{\mathbf{l}} \delta \mathbf{u} = \nabla_{\mathbf{l}} (\mathbf{u}') = \nabla_{\mathbf{x}} (\mathbf{u}'), \quad \nabla_{\mathbf{l}} \delta p = \nabla_{\mathbf{l}} (p') = \nabla_{\mathbf{x}} (p') \quad (\text{A } 2)$$

so that

$$\frac{\partial}{\partial t} \mathbf{u}' + \nabla_{\mathbf{l}} \delta \mathbf{u} \cdot \mathbf{u}' + \nabla_{\mathbf{l}} \delta p = 0. \quad (\text{A } 3)$$

Combining the equations (3.4) for  $\mathbf{u}$  and (A 3) for  $\mathbf{u}'$  we obtain for the velocity increment  $\delta \mathbf{u}$

$$\frac{\partial}{\partial t} \delta \mathbf{u} - \nabla_{\mathbf{x}} \mathbf{u} \cdot \mathbf{u} + \nabla_{\mathbf{l}} \delta \mathbf{u} \cdot \mathbf{u}' + \nabla_{\mathbf{l}} \delta p - \nabla_{\mathbf{x}} p = 0. \quad (\text{A } 4)$$

We can add  $\nabla_{\mathbf{x}} \mathbf{u}' \cdot \mathbf{u}$  and subtract  $\nabla_{\mathbf{l}} \delta \mathbf{u} \cdot \mathbf{u}$  to obtain

$$\frac{\partial}{\partial t} \delta \mathbf{u} + \nabla_{\mathbf{x}} \delta \mathbf{u} \cdot \mathbf{u} + \nabla_{\mathbf{l}} \delta \mathbf{u} \cdot \delta \mathbf{u} + \nabla_{\mathbf{l}} \delta p - \nabla_{\mathbf{x}} p = 0. \quad (\text{A } 5)$$

Again because  $p$  is independent of  $\mathbf{l}$ ,  $\nabla_{\mathbf{x}} p = \nabla_{\mathbf{l}} (\mathbf{l} \cdot \nabla_{\mathbf{x}} p)$  and we can rewrite this equation as (3.5).

Otherwise, since by (A 2)  $\nabla_{\mathbf{l}} (\delta p) = \nabla_{\mathbf{x}} p'$  we moreover have from (A 5) that

$$\frac{\partial}{\partial t} \delta \mathbf{u} + \nabla_{\mathbf{x}} \delta \mathbf{u} \cdot \mathbf{u} + \nabla_{\mathbf{l}} \delta \mathbf{u} \cdot \delta \mathbf{u} + \nabla_{\mathbf{x}} \delta p = 0, \quad (\text{A } 6)$$

which is an equivalent form of (3.5). To the two forms of the pressure contribution to the momentum balance (3.5) correspond to two forms of the pressure contribution to the energy balance (3.6):  $\nabla_{\mathbf{l}} \cdot ((\delta p - \mathbf{l} \cdot \nabla_{\mathbf{x}} p) \delta \mathbf{u})$  and  $\delta \mathbf{u} \cdot \nabla_{\mathbf{x}} \delta p = \nabla_{\mathbf{x}} \cdot (\delta \mathbf{u} \delta p)$ .

#### Relation with previous work

Relations (3.5) and (A 6) follow from the Lagrangian approach introduced by Monin & Yaglom (1971, p. 401) and recently pursued by Lundgren (2003). Consider the Lagrangian trajectory  $\mathbf{x}(t)$  of a fluid element and the reference frame translating with it. In this reference frame, the independent spatial variable is  $\mathbf{l}$  and the relative velocity field is  $\mathbf{v}(\mathbf{l}, t) = \delta \mathbf{u}(\mathbf{x}(t), \mathbf{l}, t)$ . This reference frame is translating relatively to the original Galilean reference frame with acceleration  $-\nabla_{\mathbf{x}} p(\mathbf{x}(t))$ , hence  $\mathbf{v}$  almost obeys the Euler equation; we only need to add the inertial force  $\nabla_{\mathbf{x}} p(\mathbf{x}(t))$  on the right-hand side:

$$\frac{\partial \mathbf{v}}{\partial t} + \nabla_{\mathbf{l}} \mathbf{v} \cdot \mathbf{v} = \nabla_{\mathbf{x}} p - \nabla_{\mathbf{l}} p'. \quad (\text{A } 7)$$



Relation (A 6) is obtained by returning to a fully Eulerian description where  $\mathbf{x}$  is also an independent spatial variable ( $\partial \mathbf{v} / \partial t = \partial(\delta \mathbf{u}) / \partial t + \nabla_{\mathbf{x}} \delta \mathbf{u} \cdot \mathbf{u}(\mathbf{x}, t)$ ) and using  $\nabla_{\mathbf{x}} p - \nabla_{\mathbf{I}} p' = -\nabla_{\mathbf{x}} \delta p$ .

Lundgren further transformed equation (A 7) by including the inertial force  $\nabla_{\mathbf{x}} p$  in the pressure field (Lundgren 2003) in the same way that relation (A 6) may be recast as (3.5). Expressing Lundgren's equation in a fully Eulerian description, one obtains (3.5).

The form  $\nabla_{\mathbf{x}} \cdot (\delta \mathbf{u} \delta p)$  of the pressure term is the one obtained by Hill (2002), who also includes viscous and forcing terms. Notice that Hill obtains a spatial advection at the velocity  $\mathbf{U} = (\mathbf{u}' + \mathbf{u})/2$  due to a slightly different set of independent variables: his position is not  $\mathbf{x}$  but  $\mathbf{X} = (\mathbf{x} + \mathbf{x}')/2$ . These variables were also used in Dubos & Babiano (2002). The algebra is then more symmetric and slightly simpler, especially for viscous terms. The main advantage of the independent variables  $(\mathbf{x}, \mathbf{I})$  used in the present work over the variables  $(\mathbf{X}, \mathbf{I})$  is that the relations (3.5), (3.6) have the simple physical interpretation of momentum and energy balances in the co-moving reference frame.

## REFERENCES

- BABIANO, A., BASDEVANT, C. & SADOURNY, R. 1985 Structure functions and dispersion laws in two-dimensional turbulence. *J. Atmos. Sci.* **42**, 941–949.
- BOFFETTA, G., CELANI, A. & VERGASSOLA, M. 2000 Inverse cascade in two-dimensional turbulence: deviations from Gaussianity. *Phys. Rev. E* **61**, R29–R32.
- DUBOS, T. 2001 A spatially selective parameterization for the transport of a passive or active tracer by a large scale flow. *C. R. Acad. Sci. Paris* **329**, 509–516.
- DUBOS, T. & BABIANO, A. 2002 Cascades in two-dimensional mixing: a physical space approach. *J. Fluid Mech.* **467**, 81–100.
- DUBOS, T. & BABIANO, A. 2003 Comparing the two-dimensional cascades of vorticity and a passive scalar. *J. Fluid. Mech.* **492**, 131–145.
- ELHMAIDI, D., PROVENZALE, A. & BABIANO, A. 1993 Elementary topology of two-dimensional turbulence from a Lagrangian viewpoint and single-particle dispersion. *J. Fluid Mech.* **257**, 533–558.
- HILL, R. 2002 Exact second-order structure-function relationship. *J. Fluid Mech.* **468**, 317–326.
- HUA, B. & KLEIN, P. 1998 An exact criterion for the stirring properties of nearly two-dimensional turbulence. *Physica D* **113**, 98–110.
- KOLMOGOROV, A. 1941 Local structure of turbulence in noncompressible fluid with very high Reynolds number. *Dokl. Acad. Sci.* **30** (4), 301–305.
- KRAICHNAN, R. 1967 Inertial ranges in two-dimensional turbulence. *Phys. Fluids* **10**, 1417–1423.
- LANDAU, L. & LIFSHITZ, E. 1971 *Mécanique des Fluides*. Éditions Mir.
- LAPEYRE, G., HUA, B. L. & KLEIN, P. 2001 Dynamics of the orientation of gradients of passive and active scalars in two-dimensional turbulence. *Phys. Fluids* **13**, 251–264.
- LEITH, C. 1971 Atmospheric predictability and two-dimensional turbulence. *J. Atmos. Sci.* **28**, 145–161.
- LINDBORG, E. 1999 Can the atmospheric kinetic energy spectrum be explained by two-dimensional turbulence? *J. Fluid Mech.* **388**, 259–288.
- LINDBORG, E. & ALVELIUS, K. 2000 The kinetic energy spectrum of the two-dimensional enstrophy turbulence cascade. *Phys. Fluids* **12**, 945–947.
- LUNDGREN, T. 2003 Kolmogorov turbulence by matched asymptotic expansions. *Phys. Fluids* **15**, 1074–1081.
- MCWILLIAMS, J. 1984 The emergence of isolated coherent vortices in turbulent flow. *J. Fluid Mech.* **146**, 21–43.
- MALTRUD, M. & VALLIS, G. 1991 Energy spectra and coherent structures in forced two-dimensional turbulence. *J. Fluid Mech.* **228**, 321–342.
- MONIN, S. & YAGLOM, A. 1971 *Statistical Fluid Mechanics*. MIT press.

- NIE, Q. & TANVEER, S. 1999 A note on third-order structure functions in turbulence. *Proc. R. Soc. Lond. A* **455**, 1615–1635.
- PARET, J. & TABELING, P. 1997 Experimental observation of the two-dimensional inverse energy cascade. *Phys. Rev. Lett.* **79**, 4162.
- PARET, J. & TABELING, P. 1998 Intermittency in the two-dimensional inverse cascade of energy. *Phys. Fluids* **10**, 3126–3136.
- PEDLOSKY, J. 1979 *Geophysical Fluid Dynamics*. Springer.
- PROTAS, B., BABIANO, A. & KEVLAHAN, N. K.-R. 1999 On geometrical alignment properties of two-dimensional forced turbulence. *Physica D* **128**, 169–179.